Title
Ultrabroadband infrared near-field spectroscopy and imaging of local resonators in percolative gold films

Journal
Journal of the Optical Society of America B, 36(12)

ISSN
0740-3224

Authors
Chen, Xinzhong
Zhang, Jiawei
Yao, Ziheng
et al.

Publication Date
2019-12-01

DOI
10.1364/josab.36.003315

Peer reviewed

Ultrabroadband infrared near-field spectroscopy and imaging of local resonators in percolative gold films

Xinzhong Chen[1], Jiawei Zhang[1], Ziheng Yao[1], Hans A. Bechtel[2], Michael C. Martin[2], G. L. Carr[3*], Mengkun Liu[1*]

[1] Department of Physics, Stony Brook University, Stony Brook, New York 11794, United States.

[2] Advanced Light Source Division, Lawrence Berkeley National Laboratory, Berkeley, California 94720, United States.

[3] National Synchrotron Light Source II, Brookhaven National Laboratory, Upton, New York 11973, United States.

mengkun.liu@stonybrook.edu

carr@bnl.gov

Percolation processes are ubiquitous in nature and are responsible for many critical phenomena, such as first-order phase transitions and infectious epidemic networks. The optical properties of a percolative medium can generally be captured by the effective medium approximation (EMA) when the degree of percolation and the properties of the constituent materials are properly addressed. However, the important local collective responses of nanoclusters in the deep subwavelength regime are often only phenomenologically addressed in the standard EMA formalism. A comprehensive method that measures local light-matter interactions and registers how the local responses influence global optical properties has yet to be established on a firm basis. In this letter, we use infrared nano-imaging/ spectroscopy to investigate percolative gold films at the vicinity of the critical percolation threshold. We demonstrate experimentally and theoretically that the near-field spectra yield quantitative information of the characteristic length scale of the local gold clusters and their relative oscillator strengths. As a result, EMA analysis can be augmented with near-field nano-spectroscopy to yield better

predictability of the far-field reflection spectrum at the corresponding spectral range.

1. INTRODUCTION

Percolative metal-dielectric composites possess interesting electromagnetic properties. For example, the insulator-to-metal transitions in percolative metal thin films (PMFs) yield tunable dielectric constants that are anomalously high at the vicinity of the phase percolation[1]. Among complex metal-dielectric composites, random percolative metal-dielectric thin films are exceptionally difficult to study because their nonuniform cluster size, irregular shape, and inhomogeneous distributions pose formidable obstacles for rigorous *ab initio* treatments[2,3]. In addition, local metal clusters at a length scale significantly smaller than the wavelength can play a dominant role in determining the plasmonic responses of the PMFs[4–9], which are difficult to address using areal averaging methods. Optical probes that can offer quantitative measurements of the microscopic details are therefore crucial for better modeling of the metal-insulator mixtures.

In a simple picture, PMFs can be modeled as a random arrangement of conducting bonds on an infinite grid. As the fraction of the metal distribution f increases from 0 to 1, an electrically connected network gradually forms, and the system undergoes a transition from insulating to conducting. This transition occurs at a critical fraction f_c whose value depends on many factors, such as the system dimensionality, lattice geometry, and the correlation between sites (e.g., f_c = 0.5 for two-dimensional square lattice without correlation). The macroscopic physical properties, such as film sheet conductivity, of these systems can be derived from effective approaches such as the classical effective medium approximation (EMA)[10]. Although qualitative macroscopic properties can usually be well understood through EMA, local characteristics involving mesoscale collective electron interactions are generally overlooked[11–13]. This is why metamaterials or photonic crystals, for example, cannot be described satisfactorily using conventional EMA formulations. On the contrary, the metamaterial resonances can be described well in terms of local oscillators using equivalent *LC* circuit analysis or antenna theory at the single-unit-cell level (usually the inter-cell interaction is neglected)[14]. In

the case of random PMFs, however, no unit cell can be specified, and a rigorous microscopic description is mathematically expensive. One way to solve this dilemma is to use a phenomenological and less intuitive EMA that describes the local variations of the inclusion[1,15]. Here, we demonstrate a new method to understand the local and global properties of PMFs: starting from the effective dielectric function using EMA, by incorporating the near-field-resolved local resonances into our analysis, the IR reflectance can be faithfully reproduced.

A series of gold PMFs on c-cut sapphire substrates are prepared by thermal vacuum deposition method. Their sheet resistance is closely monitored during the deposition process so that they span across the percolative threshold. This is verified by scanning electron microscope (SEM) and DC resistance measurements, where samples with similar morphology show dramatically different sheet resistances (Fig. 1(a)-(c)). Films exhibiting infinite and finite sheet resistance are classified as insulating films (IFs) and conductive films (CFs), respectively. Here we focus our attention on the optical properties of 4 (out of 9) characteristic samples with sheet resistance 20 $\Omega/\square$ (sample A), 14.5 $k\Omega/\square$ (sample B), and $\infty\ \Omega/\square$ (sample C and D). The detailed growth conditions and DC measurements of the full sample set will be reported in a separate article.

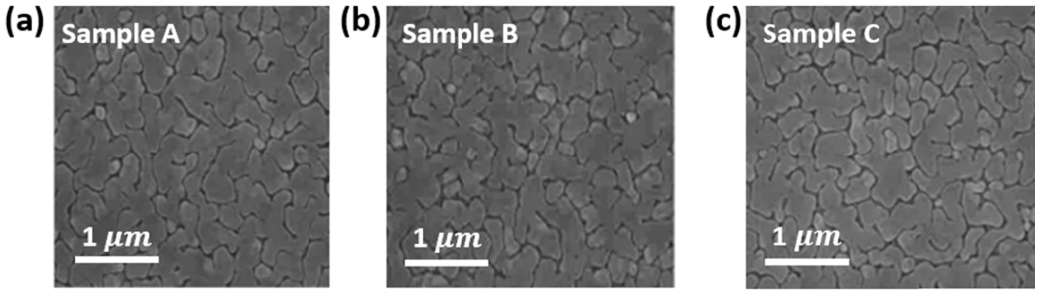

(d)

Sample label	Sheet resistance (kΩ)	Mean thickness (nm)
1 (sample D)	∞	24
2 (sample C)	∞	30
3	∞	32.5
4	∞	33
5 (sample B)	14.5	37.5
6	2.16	32.7
7	0.61	33.2
8	1.35	33
9 (sample A)	0.02	33

Fig. 1 (a)-(c) SEM images of three representative samples across the percolation threshold. (d) table for sample sheet resistance and mean thickness.

2. FAR-FIELD INFRARED SPECTROSCOPY

We first carry out conventional Fourier-transform infrared spectroscopy (FTIR) and apply EMA to interpret the far-field reflectance R. The schematic of the model is depicted in Fig. 2(a). The IR far-field reflectance spectra of the set of gold films are shown in Fig. 2(b). With increasing percolation levels, R is greatly enhanced at higher frequencies (>900 cm^{-1}) (indicated by the red arrow). The spectrum of the c-cut sapphire substrate is also included as a reference (gray curve). It is clear that the IR active phonon response of the bare sapphire substrate shows a high reflectance between 750 to 900 cm^{-1} and cutoffs at ~1000 cm^{-1} (Reststrahlen band). The spectra of the thin gold films on sapphire, on the other hand, do not show flat optical responses as from uniform metal films but instead show spectral features reminiscent of sapphire phonons (pink to red curves). There is a pronounced frequency dip at ~800 cm^{-1} which redshifts with increasing levels of percolation and diminishes for the most conducting film (Sample A).

We attribute the redshift to the interplay between sapphire phonon mode and gold plasmonic response.

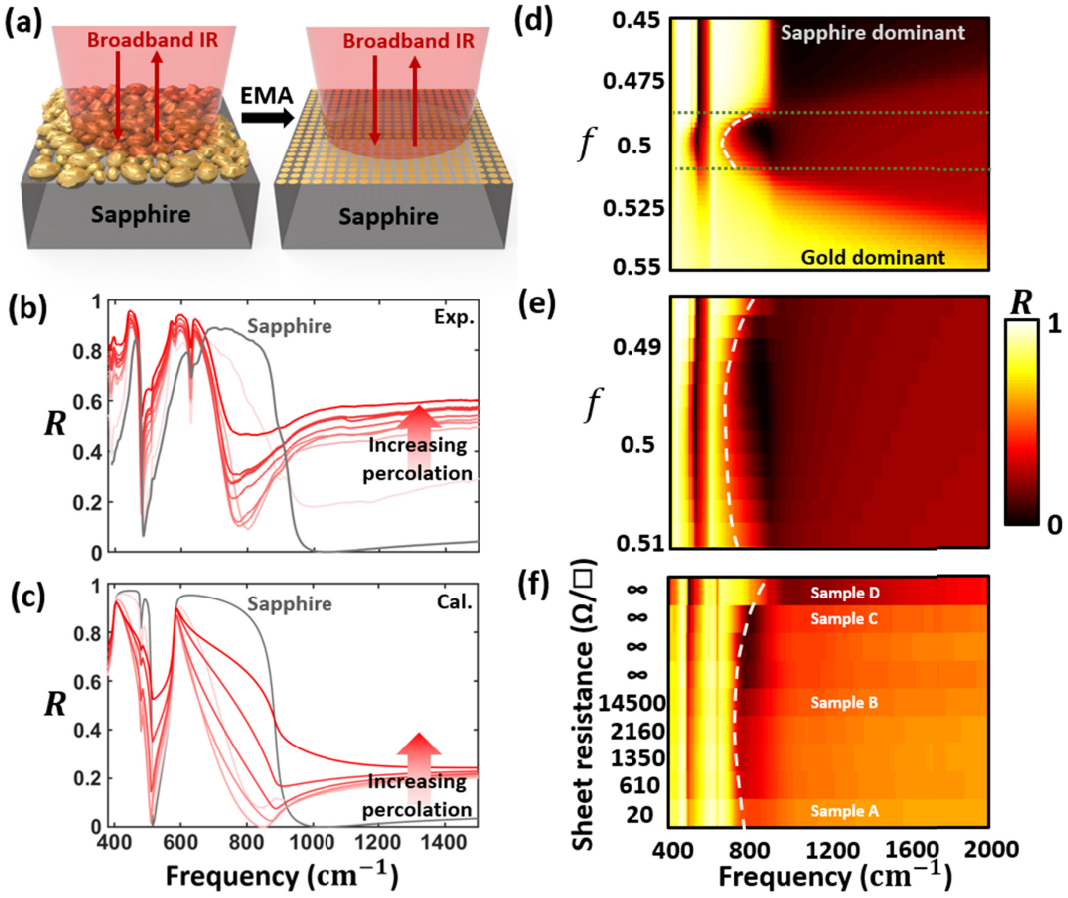

Fig. 2 (a) Schematics of percolating gold film (left) and the corresponding EMA modeling (right). (b) Far-field FTIR reflectance of a bare sapphire substrate (gray curve) and gold films on sapphire substrate (red curves). (c) Simulation of far-field reflectance in (b) using EMA with f taken between 0.49 (below percolation) and 0.51 (above percolation). (d) Calculation of IR reflectance as a function of frequency and filling fraction f. (e) A zoom-in of (d) close to $f_c = 0.5$. (f) Experimental data in (b) replotted as a function of frequency and sheet resistance, in comparison with (e).

To understand the far-field IR spectra of the percolating gold films, a simple two-dimensional Bruggeman EMA is employed. We first approximate the gold layer as an effective medium that is a mixture of gold and air. According to Bruggeman's formulation with circular inclusions, we have

$$\frac{f(\varepsilon_g-\varepsilon_{\text{eff}})}{\varepsilon_g+\varepsilon_{\text{eff}}}+\frac{(1-f)(\varepsilon_{\text{air}}-\varepsilon_{\text{eff}})}{\varepsilon_{\text{air}}+\varepsilon_{\text{eff}}}=0\,, \tag{1}$$

where f is the filling fraction of gold[12,16,17]. In this model, the effective percolation threshold is $f_c = 0.5$, which is lower than the expected value $f_c^{exp} > 0.9$ estimated from SEM images of our films. Nonetheless, this approach provides a reasonable qualitative description and a more intuitive picture than other complex models. We note here that since the gold clusters have a uniform and isotropic distribution, for simplicity, we use an EMA with isotropic circular inclusions and avoid other geometries such as elliptical and needle-like shapes. This also "turns off" the inter-cluster interactions[1].

As shown in Fig. 2(c), the far-field reflectance is calculated using the multilayer Fresnel equation considering a layer with EMA permittivity ε_{eff} on top of a sapphire substrate. Gold is described by a conventional Drude model and the complex dielectric permittivity is given by

$$\varepsilon_g = 1-\frac{\omega_p^2}{\omega^2+i\gamma\omega}\,, \tag{2}$$

where $\gamma = \frac{1}{\tau}$ is the relaxation rate and ω_p is the plasma frequency[18]. Over the years inconsistent values of both ω_p and γ have been experimentally measured mainly due to sample growth and experimental conditions[19,20]. Here we adopt the values from the relatively new study by Olmon *et al.*[21] where τ is found to be $\sim 14\,fs$ and $\omega_p = 8.45\,eV$. On the other hand, sapphire exhibits anisotropy where the dielectric functions for ordinary (o) and extraordinary (e) axes are different. The dielectric function is given by

$$\varepsilon_\mu = \varepsilon_{\infty,\mu}\prod_j \frac{\omega_{jLO,\mu}^2-\omega^2-i\gamma_{jLO,\mu}\omega}{\omega_{jTO,\mu}^2-\omega^2-i\gamma_{jTO,\mu}\omega}, \tag{3}$$

where $\mu = o$ ($\mu = e$) for ordinary (extraordinary) axes, $\omega_{jLO,\mu}$ ($\omega_{jTO,\mu}$) and $\gamma_{jLO,\mu}$ ($\gamma_{jTO,\mu}$) are the resonant frequency and relaxation rate of the j-th longitudinal (transverse) optical mode. Numeric values of those parameters can be found in the literature[22,23]. The reflectance is therefore calculated as

$$R = |r|^2 = \left|\frac{r^{01}+r^{12}e^{2i\theta}}{1+r^{01}r^{12}e^{2i\theta}}\right|^2, \tag{4}$$

where $r^{ij} = \frac{n_i - n_j}{n_i + n_j}$ stands for reflection coefficient between the i-th and j-th layer and $\theta = \frac{2\pi n_1 d}{\lambda}$ with d the film thickness and λ the free space wavelength. Realistically the mean film thickness varies from 24 nm to 37.5 nm. As the thickness does not drastically change the calculation result, here for simplicity, we set $d = 30\,nm$ without loss of generality.

As f increases across the percolation threshold, the spectrum changes dramatically and agrees qualitatively with the experimental data (Fig. 1(b)). In particular, the redshift of the dip of the resonance is reproduced well by the current model, reaching ~800 cm^{-1} at $f_c = 0.5$. This redshift in the far-field responses is therefore likely to be a manifestation of the percolation behavior. To better illustrate this, we plot the calculated IR reflectance as a function of frequency and f in Fig. 2(d) and zoom into the redshifted region around $f_c = 0.5$ in Fig. 2(e). As shown in Fig. 2(f), experimental data replotted as a function of frequency and sheet resistance show the same trend as in Fig. 2(e). Therefore, the general far-field IR responses in our gold films are qualitatively characterized by EMA with f close to $f_c = 0.5$. However, the long spectral tails calculated by EMA above the ~900 cm^{-1} range [Fig. 1(c)] significantly underestimate the IR reflectance from experiments [Fig. 1(b)]. As we will show below, the local plasmonic behavior of the gold clusters emerge as a dominant factor at frequencies above 900 cm^{-1} and contribute to the spectral weight lost in EMA. These local optical responses are expected to demonstrate strong variations depending on the local geometries of the granular domains and are totally averaged out in the far-field measurements[24–27].

3. NEAR-FIELD INFRARED SPECTROSCOPY AND NANO-IMAGING

Near-field nano-imaging and nano-spectroscopy are therefore useful in probing the local optical responses of the gold clusters and revealing the characteristics of their plasmonic behaviors[28–30]. The near-field experiment is schematically shown in Fig. 3(a). In the terahertz (THz) region ($\lambda \approx 300\,\mu m$), nano-imaging reveals a rather homogeneous response in all samples. In Figs. 3(b) and (c), we show two representative THz s-SNOM images of samples A (20 Ω/□) and D (∞). It is worth noting that although optical inhomogeneity is absent, the global THz near-field signal levels differ

considerably between the two films: the one with low sheet resistance yields a nearly threefold increase in the THz signal, indicating the drastically different low-frequency film conductivity. In the mid-IR region ($\lambda = 11$ μm), on the other hand, strong optical inhomogeneities are discovered in all films, similar to presvious reports using shorted wavelength excitation [9,25,31–33]. Three representative samples are shown in Figs. 3(d)–(f), in which local IR responses vary dramatically over a length scale of a few micrometers. The atomic force microscope (AFM) images acquired simultaneously in the same set of samples [Figs. 3(g)–(i)] do not show topographical variations on the same micrometer scale of the near-field "hot spots".

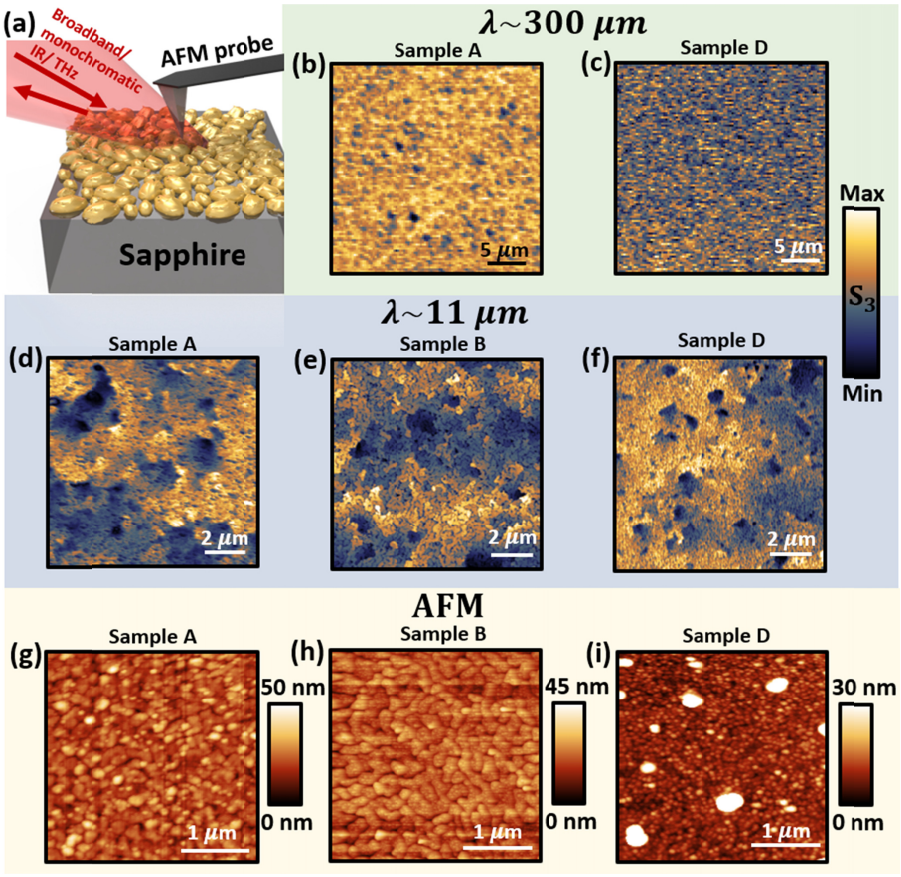

Fig. 3 (a) Schematic illustration of scattering-type scanning near-field optical microscopy (s-SNOM) experiments using broadband or monochromatic light sources. (b) and (c) THz s-SNOM images of samples A and D. (d)–(f) IR s-SNOM images of samples A, B, and D. (g)–(i) AFM topographic images of samples A, B, and D.

To understand the optical inhomogeneities in the monochromatic near-field images, we performed broadband nano-spectroscopy based on a similar setup[34]. Representative nano-IR spectra were taken at random locations within 10 μm ×10 μm scan area on samples A (Fig. 4(a)), B (Fig. 4(b)), C (Fig. 4(c)), and D (Fig. 4(d)). All the near-field spectra are normalized to that of a thick gold film to yield a physically meaningful relative amplitude. From Fig. 4 (a)-(d), three major observations are evident: (1) the sapphire phonon response is still visible but reduced in strength; (2) nano-IR spectra vary from one location to another, with the variation being more dramatic in the CFs than the IFs; (3) multiple resonant peaks at high frequencies (900–1400 cm^{-1}) can be identified in the CFs [marked by arrows in Fig. 4(a)], but are less prominent in the IFs. Those spectral peaks are absent in the far-field spectra in Fig. 2(b) and are believed to originate from the local plasmonic resonators formed by gold clusters.

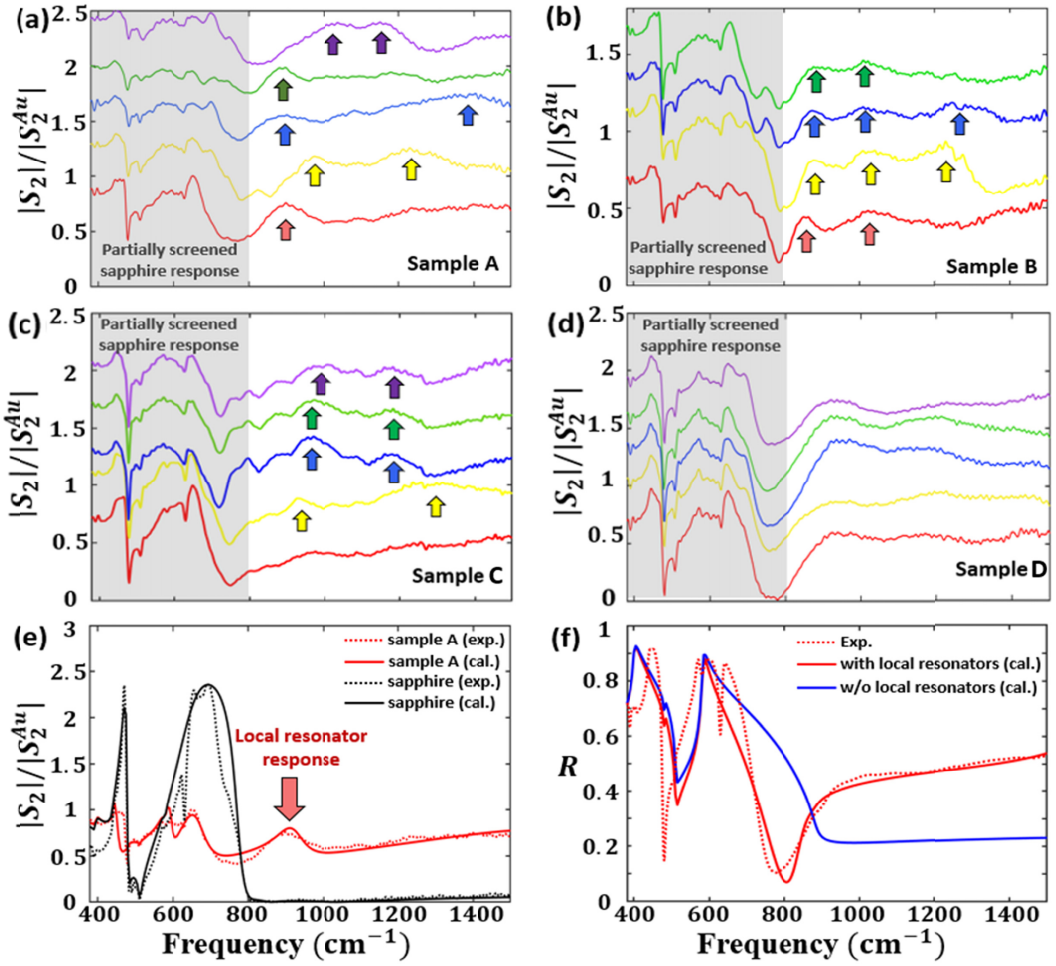

Fig. 4 (a)-(d) Near-field spectra taken at random locations in two CFs (sample A and B) and two IFs (sample C and D), respectively. All curves are shifted for clarity. Arrows in (a), (b), and (c) mark the local resonance peaks. (e) IR near-field spectra taken from a CF and bare sapphire compared with theoretically calculated spectra. (f) Far-field reflectance using only EMA (blue curve) and EMA with local resonators (red curve). For comparison, one experimental spectrum from Fig. 1(b) is also shown (red dashed curve).

4. THEORETICAL MODELLING

We propose that the s-SNOM probes the local permittivity of the gold films, which can be described by the sum of the macroscopic effective medium background and local Lorentzian resonators:

$$\varepsilon_g^n = \varepsilon_{\text{eff}} + \sum_j \frac{s_j}{\omega_{oj}^2 - \omega^2 + i\omega\gamma_j}, \tag{5}$$

where s_j is the oscillator strength, ω_{0j} is the resonant frequency, and γ_j is the damping coefficient. ε_{eff} is given by equation (1). We used $f = 0.5$ in the following calculation. Higher (lower) *f* corresponds to more metallic (insulating) behavior, which only affects the overall signal intensity in the near-field measurement but has minimal influence on the resonance. This phenomenon has been observed similarly in artificial percolation system with scanning microwave impedance microscopy[35]. These resonators emerge because of the strong plasmonic resonances. The near-field response can be calculated analytically or numerically by modeling the AFM tip as a point dipole, elongated spheroid, or cone[23,36–41]. Here we adopt the finite-dipole model as detailed in the work by Cvitkovic *et al.*[36]. The essence is that the scattered field, which is experimentally detected in s-SNOM, is given by

$$E_{\text{sca}} \propto \left(1 + r_p\right)^2 \alpha_{\text{eff}}, \tag{6}$$

where $\alpha_{\text{eff}}(\beta)$ is the tip effective polarizability that is proportional to the induced dipole moment on the tip. α_{eff} reflects how strong the near-field tip-sample interaction is. In the dipole scattering framework, the scattered field is proportional to the dipole moment thus proportional to α_{eff}. r_p is the p-polarized reflection coefficient and $\left(1 + r_p\right)^2$ is commonly referred to as the "far-field factor" due to direct surface reflection. This factor is found to play a minor role so is ignored for simplicity[42]. β is the sample response

function, which is related to sample permittivity. For bulk samples with permittivity ε, $\beta = (\varepsilon - 1)/(\varepsilon + 1)$ is the quasi-static reflection coefficient. For our gold thin film/sapphire structure, ε as an approximation can be interpreted as an effective value derived directly from the Fresnel equation

$$\varepsilon^* = \varepsilon_g^n \frac{\varepsilon_s + \varepsilon_g^n \tanh(q^* d)}{\varepsilon_g^n + \varepsilon_s \tanh(q^* d)}, \tag{7}$$

where $\varepsilon_s = \sqrt{\varepsilon_o \varepsilon_e}$ is the averaged permittivity of sapphire[42], d is the film thickness, and $q^* \sim 1/(10a)$ is the phenomenological effective in-plane momentum[43]. For a direct comparison with the experimental near-field spectrum, α_{eff} needs to be demodulated to 2nd harmonics of the tip tapping frequency and normalized to a gold reference. As a demonstration, in Fig. 4(e) we compare our model calculation (solid curves)

$$S_2 \propto (\alpha_{\text{eff}})_{2nd} / (\alpha_{\text{reference}})_{2nd} \tag{8}$$

to experimental data (dashed curves). The near-field spectra of film A (red) and sapphire substrate (black) are well fitted. Most importantly, the partially screened sapphire phonon responses and the local resonators of the gold films can be well reproduced.

From the above analysis, extra information of the local resonators that is missing from the macroscopic EMA modeling can be readily extracted from the near-field investigation. These local resonators contribute to the far-field spectra significantly, similar to an array of antennas. It is therefore reasonable to reconstruct better modeling of the far-field reflectance from the obtained near-field information. That is, the contributions from the local resonators should be included in the EMA permittivity. The resonance frequency ω_{0j}, oscillator strength s_j, and the damping coefficient γ_j of the local resonators are expected to follow a specific distribution function $D(\omega_0, s, \gamma)$. That is, the macroscopic permittivity of the gold film is then given by

$$\varepsilon'_{\text{eff}} = \varepsilon_{\text{eff}} + \int_{\omega_{min}}^{\omega_{max}} D(\omega_0, s, \gamma) \frac{s}{\omega_0^2 - \omega^2 + i\gamma} \, d\omega_0 \tag{9}$$

instead of simply ε_{eff} given by equation (1). The exact form of $D(\omega_0, s, \gamma)$ is complex and intimately related to the particular gold films under investigation. As a proof-of-

concept demonstration, here we assume that $D(\omega_0, s, \gamma)$ follows a constant distribution in the range from $\omega_{min} = 850\ cm^{-1}$ to $\omega_{max} = 1600\ cm^{-1}$. In this case $D = \frac{1}{\omega_{max} - \omega_{min}}$. We take s and γ as constants for all resonators, but in principle they can be varied as well. Far-field reflectance calculated using $\varepsilon'_{\text{eff}}$ (red curve) and ε_{eff} (blue curve) are shown in Fig. 4(f). With local resonators added to the picture (red curve) in this simplistic consideration, the spectral response is already significantly more consistent with the experimental data (dashed red curve). As can be observed in Fig. 4(a)-(d), the resonators are generally weaker in IFs than in the CFs, which also explains the lower far-field reflectance in IF above ~900 cm^{-1} (Fig. 1(b)). A flowchart of our improved fitting procedure using a combination of the near-field and far-field data is summarized in Fig. 5.

5. CONCLUSION AND SUMMARY

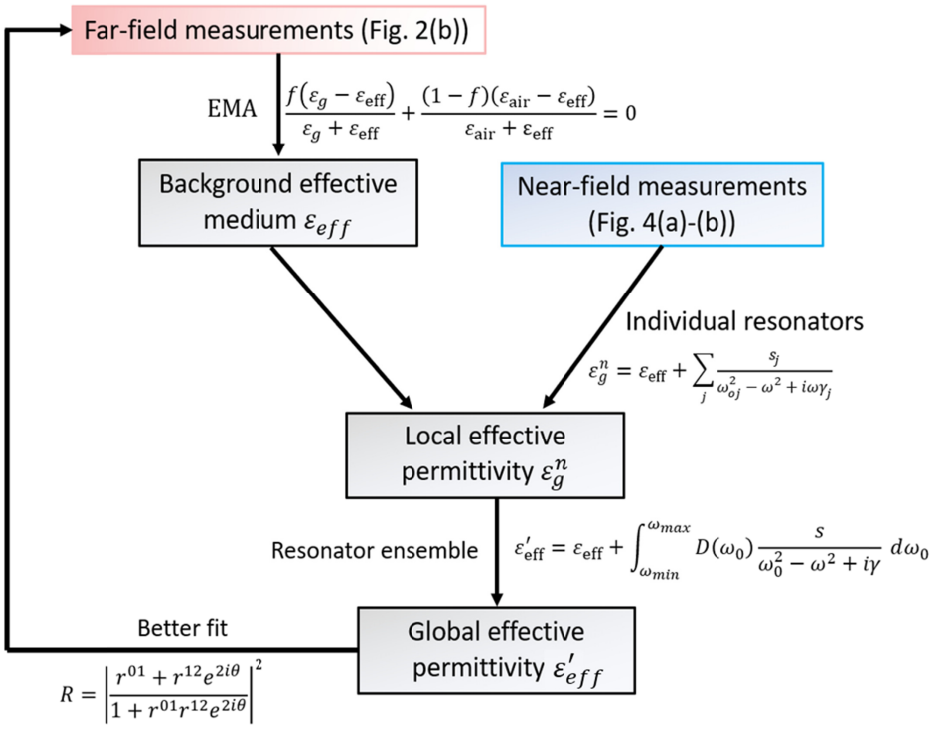

Fig. 5 Flow chart of the combined far-field/ near-field analysis to yield a better understanding of the PMFs.

To conclude, we have investigated gold PMFs on sapphire substrates with far-field FTIR, IR and THz nanoimaging, and IR nano-spectroscopy. A wide range of frequencies from the mid-IR to the THz regime have been covered for the first time. Cluster-like

inhomogeneous optical responses are clearly observed at mid-IR frequencies but are completely absent at much longer wavelengths in the THz regime. The elevated far-field reflectance above ~900 cm^{-1} is found to be a direct consequence of the collective response of micro-resonators formed by the local gold clusters. Standard EMA methods do not address the local resonances therefore underestimates the IR reflectance at certain frequency ranges. We conclude that a collaborative investigation of both far-field and near-field properties paints a more complete picture of the system under study: EMA provides a general background effective permittivity of the percolating gold films, which can be augmented by contributions from local resonators probed by near-field optics. This work can be instructional for future studies of random or quasi-random photonic structures using near-field methods, which are potentially important for applications of field enhancement, light trapping, and energy storage[44,45].

Acknowledgment

This work is supported by the National Science Foundation under Grant No. DMR-1904576. This research used Beamlines 2.4 and 5.4 of the Advanced Light Source, which is a DOE Office of Science User Facility under Contract No. DE-AC02-05CH11231.

References

1. S. De Zuani, M. Rommel, B. Gompf, A. Berrier, J. Weis, and M. Dressel, "Suppressed Percolation in Nearly Closed Gold Films," ACS Photonics **3**(6), 1109–1115 (2016).

2. D. Stauffer and A. Aharony, *Introduction to Percolation Theory* (Taylor & Francis, 1985).

3. V. K. S. Shante and S. Kirkpatrick, "An introduction to percolation theory," Adv. Phys. **20**(85), 325–357 (1971).

4. J. . Sipe and R. W. Boyd, "Nonlinear susceptibility of composite optical materials in the Maxwell Garnett model," Phys. Rev. A **46**(3), (1992).

5. R. F. Voss, R. B. Laibowitz, and E. I. Allessandrini, "Fractal (Scaling) Clusters in Thin

Gold Films near the Percolation Threshold," Phys. Rev. Lett. **49**(19), 1441–1444 (1982).

6. V. Krachmalnicoff, E. Castanié, Y. De Wilde, and R. Carminati, "Fluctuations of the Local Density of States Probe Localized Surface Plasmons on Disordered Metal Films," Phys. Rev. Lett. **105**(18), 183901 (2010).

7. M. Hövel, B. Gompf, and M. Dressel, "Dielectric properties of ultrathin metal films around the percolation threshold," Phys. Rev. B **81**(3), 035402 (2010).

8. M. Naruse, S.-J. Kim, T. Takahashi, M. Aono, K. Akahane, M. D'Acunto, H. Hori, L. Thylén, M. Katori, and M. Ohtsu, "Percolation of optical excitation mediated by near-field interactions," Phys. A Stat. Mech. its Appl. **471**, 162–168 (2017).

9. M. D'Acunto, F. Fuso, R. Micheletto, M. Naruse, F. Tantussi, and M. Allegrini, "Near-field surface plasmon field enhancement induced by rippled surfaces," Beilstein J. Nanotechnol. **8**(1), 956–967 (2017).

10. M. Walther, D. G. Cooke, C. Sherstan, M. Hajar, M. R. Freeman, and F. A. Hegmann, "Terahertz conductivity of thin gold films at the metal-insulator percolation transition," Phys. Rev. B **76**(12), 125408 (2007).

11. J. E. Spanier and I. P. Herman, "Use of hybrid phenomenological and statistical effective-medium theories of dielectric functions to model the infrared reflectance of porous SiC films," Phys. Rev. B **61**(15), 10437–10450 (2000).

12. G. A. Niklasson, C. G. Granqvist, and O. Hunderi, "Effective medium models for the optical properties of inhomogeneous materials," Appl. Opt. **20**(1), 26 (1981).

13. D. Stroud, "Generalized effective-medium approach to the conductivity of an inhomogeneous material," Phys. Rev. B **12**(8), 3368–3373 (1975).

14. J. D. Baena, J. Bonache, F. Martin, R. M. Sillero, F. Falcone, T. Lopetegi, M. A. G. Laso, J. Garcia-Garcia, I. Gil, M. F. Portillo, and M. Sorolla, "Equivalent-circuit models for split-ring resonators and complementary split-ring resonators coupled to planar transmission lines," IEEE Trans. Microw. Theory Tech. **53**(4), 1451–1461 (2005).

15. K. W. Jacobsen, J. K. Norskov, and M. J. Puska, "Interatomic interactions in the effective-medium theory," Phys. Rev. B **35**(14), 7423–7442 (1987).

16. R. Landauer, "Electrical conductivity in inhomogeneous media," in *AIP Conference*

Proceedings (AIP, 1978), **40**(1), pp. 2–45.

17. M. Khardani, M. Bouaïcha, and B. Bessaïs, "Bruggeman effective medium approach for modelling optical properties of porous silicon: comparison with experiment," Phys. status solidi **4**(6), 1986–1990 (2007).

18. M. Dressel, G. Gruener, and G. F. Bertsch, "Electrodynamics of Solids: Optical Properties of Electrons in Matter," Am. J. Phys. **70**(12), 1269–1270 (2002).

19. J. E. Nestell and R. W. Christy, "Derivation of Optical Constants of Metals from Thin-Film Measurements at Oblique Incidence," Appl. Opt. **11**(3), 643 (1972).

20. P. B. Johnson and R. W. Christy, "Optical Constants of the Noble Metals," Phys. Rev. B **6**(12), 4370–4379 (1972).

21. R. L. Olmon, B. Slovick, T. W. Johnson, D. Shelton, S. Oh, G. D. Boreman, and M. B. Raschke, "Optical dielectric function of gold," Phys. Rev. B **86**(23), 235147 (2012).

22. S. Zeidler, T. Posch, and H. Mutschke, "Optical constants of refractory oxides at high temperatures," Astron. Astrophys. **553**, A81 (2013).

23. B.-Y. Jiang, L. M. Zhang, A. H. Castro Neto, D. N. Basov, and M. M. Fogler, "Generalized spectral method for near-field optical microscopy," J. Appl. Phys. **119**(5), 054305 (2016).

24. M. I. Stockman, S. V Faleev, and D. J. Bergman, "Localization versus Delocalization of Surface Plasmons in Nanosystems: Can One State Have Both Characteristics?," Phys. Rev. Lett. **87**(16), 167401 (2001).

25. S. Ducourtieux, V. A. Podolskiy, S. Grésillon, S. Buil, B. Berini, P. Gadenne, A. C. Boccara, J. C. Rivoal, W. D. Bragg, K. Banerjee, V. P. Safonov, V. P. Drachev, Z. C. Ying, A. K. Sarychev, and V. M. Shalaev, "Near-field optical studies of semicontinuous metal films," Phys. Rev. B **64**(16), 165403 (2001).

26. J. Laverdant, S. Buil, B. Bérini, and X. Quélin, "Polarization dependent near-field speckle of random gold films," Phys. Rev. B **77**(16), 165406 (2008).

27. A. Cazé, R. Pierrat, and R. Carminati, "Spatial Coherence in Complex Photonic and Plasmonic Systems," Phys. Rev. Lett. **110**(6), 063903 (2013).

28. X. Chen, D. Hu, R. Mescall, G. You, D. N. Basov, Q. Dai, and M. Liu, "Modern

Scattering‐Type Scanning Near‐Field Optical Microscopy for Advanced Material Research," Adv. Mater. **1804774**, 1804774 (2019).

29. J. Chen, P. Albella, Z. Pirzadeh, P. Alonso-González, F. Huth, S. Bonetti, V. Bonanni, J. Åkerman, J. Nogués, P. Vavassori, A. Dmitriev, J. Aizpurua, and R. Hillenbrand, "Plasmonic Nickel Nanoantennas," Small **7**(16), 2341–2347 (2011).

30. B. J. Bohn, M. Schnell, M. A. Kats, F. Aieta, R. Hillenbrand, and F. Capasso, "Near-Field Imaging of Phased Array Metasurfaces," Nano Lett. **15**(6), 3851–3858 (2015).

31. R. Carminati, A. Cazé, D. Cao, F. Peragut, V. Krachmalnicoff, R. Pierrat, and Y. De Wilde, "Electromagnetic density of states in complex plasmonic systems," Surf. Sci. Rep. **70**(1), 1–41 (2015).

32. S. Grésillon, L. Aigouy, A. C. Boccara, J. C. Rivoal, X. Quelin, C. Desmarest, P. Gadenne, V. A. Shubin, A. K. Sarychev, and V. M. Shalaev, "Experimental Observation of Localized Optical Excitations in Random Metal-Dielectric Films," Phys. Rev. Lett. **82**(22), 4520–4523 (1999).

33. J. Zhong, A. Chimeh, A. Korte, F. Schwarz, J. Yi, D. Wang, J. Zhan, P. Schaaf, E. Runge, and C. Lienau, "Strong Spatial and Spectral Localization of Surface Plasmons in Individual Randomly Disordered Gold Nanosponges," Nano Lett. **18**(8), 4957–4964 (2018).

34. O. Khatib, H. A. Bechtel, M. C. Martin, M. B. Raschke, and G. L. Carr, "Far Infrared Synchrotron Near-Field Nanoimaging and Nanospectroscopy," ACS Photonics **5**(7), 2773–2779 (2018).

35. H. Thierschmann, H. Cetinay, M. Finkel, A. J. Katan, M. P. Westig, P. Van Mieghem, and T. M. Klapwijk, "Local electrodynamics of a disordered conductor model system measured with a microwave impedance microscope," Arxiv (1), 1–19 (2019).

36. A. Cvitkovic, N. Ocelic, and R. Hillenbrand, "Analytical model for quantitative prediction of material contrasts in scattering-type near-field optical microscopy," Opt. Express **15**(14), 8550 (2007).

37. A. S. McLeod, P. Kelly, M. D. Goldflam, Z. Gainsforth, A. J. Westphal, G. Dominguez, M. H. Thiemens, M. M. Fogler, and D. N. Basov, "Model for quantitative tip-enhanced spectroscopy and the extraction of nanoscale-resolved optical constants," Phys. Rev. B

90(8), 085136 (2014).

38. S. T. Chui, X. Chen, M. Liu, Z. Lin, and J. Zi, "Scattering of electromagnetic waves from a cone with conformal mapping: Application to scanning near-field optical microscope," Phys. Rev. B **97**(8), 081406 (2018).

39. F. Keilmann and R. Hillenbrand, "Near-field microscopy by elastic light scattering from a tip.," Philos. Trans. A. Math. Phys. Eng. Sci. **362**(1817), 787–805 (2004).

40. X. Chen, C. F. B. Lo, W. Zheng, H. Hu, Q. Dai, and M. Liu, "Rigorous numerical modeling of scattering-type scanning near-field optical microscopy and spectroscopy," Appl. Phys. Lett. **111**(22), 223110 (2017).

41. R. Esteban, R. Vogelgesang, and K. Kern, "Full simulations of the apertureless scanning near field optical microscopy signal: achievable resolution and contrast," Opt. Express **17**(4), 2518 (2009).

42. L. M. Zhang, G. O. Andreev, Z. Fei, A. S. McLeod, G. Dominguez, M. Thiemens, A. H. Castro-Neto, D. N. Basov, and M. M. Fogler, "Near-field spectroscopy of silicon dioxide thin films," Phys. Rev. B **85**(7), 075419 (2012).

43. B. Hauer, A. P. Engelhardt, and T. Taubner, "Quasi-analytical model for scattering infrared near-field microscopy on layered systems," Opt. Express **20**(12), 13173 (2012).

44. V. Yannopapas, "Negative refraction in random photonic alloys of polaritonic and plasmonic microspheres," Phys. Rev. B **75**(3), 035112 (2007).

45. F. Pratesi, M. Burresi, F. Riboli, K. Vynck, and D. S. Wiersma, "Disordered photonic structures for light harvesting in solar cells," Opt. Express **21**(S3), A460 (2013).